2mic

NASA TECHNICAL NOTE

NASA TN D-7421

A SIMPLIFIED HOLOGRAPHIC-INTERFEROMETRY TECHNIQUE FOR REAL-TIME FLOW VISUALIZATION AND ANALYSIS

by Shiela Ann T. Long, Robert C. Spencer, and Don M. Robinson

Langley Research Center
Hampton, Va. 23665

NATIONAL AERONAUTICS AND SPACE ADMINISTRATION • WASHINGTON, D. C. • MARCH 1974

1. Report No. NASA TN D-7421	2. Government Accession No.	3. Recipient's Catalog No.
4. Title and Subtitle A SIMPLIFIED HOLOGRAPHIC-INTERFEROMETRY TECHNIQUE FOR REAL-TIME FLOW VISUALIZATION AND ANALYSIS		5. Report Date March 1974 6. Performing Organization Code
7. Author(s) Sheila Ann T. Long, Robert C. Spencer, and Don M. Robinson		8. Performing Organization Report No. L-9114
9. Performing Organization Name and Address NASA Langley Research Center Hampton, Va. 23665		10. Work Unit No. 879-11-36-01 11. Contract or Grant No.
12. Sponsoring Agency Name and Address National Aeronautics and Space Administration Washington, D.C. 20546		13. Type of Report and Period Covered Technical Note 14. Sponsoring Agency Code
15. Supplementary Notes		

16. Abstract

A holographic-interferometry technique for flow visualization and analysis that produces real-time moiré fringes is described from both experimental and application considerations. It has three chief advantages: Real-time data for continuous observation and photography, ease of optical adjustment, and capability of using ordinary-glass test-section windows without affecting the results.

A theoretical discussion is presented describing the formation of the fringes in holographic terms and then comparing this result to that which is obtained from a conventional moiré approach. A discussion on obtaining density information from the fringe patterns is also included.

17. Key Words (Suggested by Author(s))	18. Distribution Statement
Holography Interferometry Flow visualization Moiré fringes Real time	Unclassified – Unlimited STAR Category 23

19. Security Classif. (of this report)	20. Security Classif. (of this page)	21. No. of Pages	22. Price*
Unclassified	Unclassified	~~37~~ 40	$3.25

*For sale by the National Technical Information Service, Springfield, Virginia 22151

A SIMPLIFIED HOLOGRAPHIC-INTERFEROMETRY TECHNIQUE FOR REAL-TIME FLOW VISUALIZATION AND ANALYSIS

By Sheila Ann T. Long, Robert C. Spencer,
and Don M. Robinson
Langley Research Center

SUMMARY

A holographic-interferometry technique for flow visualization and analysis that produces real-time moiré fringes is described from both experimental and application considerations. It has three chief advantages: Real-time data for continuous observation and photography, ease of optical adjustment, and capability of using ordinary-glass test-section windows without affecting the results.

A theoretical discussion is presented describing the formation of the fringes in holographic terms and then comparing this result to that which is obtained from a conventional moiré approach. A discussion on obtaining density information from the fringe patterns is also included.

INTRODUCTION

Knowledge of the flow characteristics around wind-tunnel models is required in aerodynamic and aerospace research. Shadowgraph and schlieren techniques render qualitative analyses of the flow; however, they cannot be used conveniently to determine the density changes quantitatively. The density changes may be determined by probes, but the presence of the probes distorts the original flow pattern.

If it is necessary to determine the density changes without distorting the flow, interferometry is a means. Aerodynamicists, however, have been reluctant to use interferometers because of the inherent difficulties encountered. A conventional interferometer requires high-quality transmission optical components and high-precision mechanical adjustments. Wind-tunnel vibrations, mechanical and acoustic, can destroy the required alinement of the interferometer.

One technique which may be used to circumvent some of these problems is holographic interferometry. Considerable use of this technique has been made in recent years for examining a variety of engineering problems. For applying this technique to

characterize flow phenomena, several holographic schemes are available, each one having its own advantages and disadvantages.

The first is double-exposure holography (refs. 1 and 2). In this technique variations in an object distribution (e.g., a flow field) are recorded as two separate exposures on the same hologram, one exposure with the flow absent and one with the flow present. Reconstruction of the hologram then generates an interferometric comparison (either finite fringe or infinite fringe) between the two conditions. This procedure, of course, has no real-time information, since the interferometric data correspond to the phase difference in the object distribution at two specific times (i.e., at the times of the first and second exposures). An advantage of this method is that it can be applied in a high vibration-noise environment by using a pulsed laser for the illumination source.

A variation of this technique is to record the two flow conditions on separate holograms and then to superpose them in exact register during the reconstruction (ref. 3). This technique has the same advantages as the previous technique, with the additional flexibility that, in finite-fringe interferometry, the background-fringe separation can be varied as a postexposure procedure by simply rotating one of the holograms with respect to the other. An advantage to this is that the apparent sensitivity of the interferometer can be varied by adjusting the spacing of the background fringes. The term "apparent" is used since, essentially, the sensitivity of all interferometers is the same; that is, if all conditions remain the same, an optical-path change of 1 wavelength causes the fringe pattern to be displaced by one fringe in any interferometer. The apparent sensitivity, however, can be altered by adjusting the spatial frequency of the fringes; a phase shift in an interferometer is more noticeable when the system is adjusted for broad fringes than it is for narrow fringes.

A third technique which may be employed in holographic interferometry is the reconstructed-beam, real-time-beam technique (ref. 4). This differs from the two techniques mentioned above in that only the initial object distribution (i.e., no flow) is stored in the hologram. Interferometric information between the no-flow and flow conditions is obtained by superposing the reconstructed no-flow wave field with the real-time-flow wave field. An advantage of this technique is that the interferometric data are real time. The background fringes for the finite-fringe interferograms are generated by rotating a prism in one of the real-time beams. Hence, for a finite-fringe display, the advantageous feature of variable postexposure fringe spacing is again realized. The primary disadvantage to this technique is that it is more sensitive than the other two to vibration-noise environments.

The technique reported in the present paper is best described in terms of this third technique. Specifically, a two-beam stored holographic grid recorded under the no-flow condition is reconstructed and superposed upon a two-beam real-time grid. The inter-

action of the two grids generates an interference pattern characteristic of an interferometer. If a flow or other perturbation is then introduced into either one of the two real-time beams, a perturbation in the fringe pattern results. This technique has the same advantages as the reconstructed-beam, real-time-beam technique previously described. An additional feature of the technique reported in this paper, however, is found in the different procedure which is used to generate the finite-fringe interferograms. For this, the hologram is simply rotated so that the two grids (i.e., the stored holographic grid and the real-time grid) are inclined with respect to each other. The resulting background fringes generated are thus of the same form as would be obtained if two material grids were so inclined; namely, moiré fringes.

Included in this paper is a description of this holographic-interferometry technique from both experimental and application considerations. In addition, a theoretical discussion is presented describing the formation of the fringes in holographic terms and then comparing this result to that which is obtained from a conventional moiré approach. A short discussion on obtaining density information from the fringe patterns is also included. Some of the information concerning the experimental aspects of the study has been reported previously (ref. 5).

SYMBOLS

A	amplitude of general wave field
A_o	amplitude of object wave field
A_r	amplitude of reference wave field
A_t	reconstructed amplitude using both reference and object beam illumination
A_t'	reconstructed amplitude using both reference and object beam illumination after rotation of hologram
C_1, C_2, C_3	parameters depending on A_r and A_o
d	spacing of stored holographic grid lines
e	spacing of real-time grid lines
f	spatial frequency of undisturbed moiré fringes

$f_{X'}, f_{Y'}$	X'- and Y'-components of f
h	a fixed value of η
I	irradiance of general wave field
I_o	irradiance of fringes appearing in object beam under flow condition
I_t	irradiance of fringes appearing in both reference and object beams under no-flow condition
K	Gladstone-Dale constant
$k_{X'}, k_{Y'}, k_Z$	propagation numbers associated with X'-, Y'-, and Z-directions, respectively
L	spacing of undisturbed moiré fringes
ℓ	length of test section
m	integer numbering dark fringes
n	refractive index under flow condition
n_0	refractive index under no-flow condition
ds	differential arc length for deflected light ray
X,Y	orthogonal axes in plane of hologram
Z	axis mutually orthogonal to X and Y and perpendicular to plane of hologram
x,y,z	point on hologram
X',Y'	orthogonal axes in plane of hologram during reconstruction
x',y'	point on recording plane during reconstruction

x_0', y_0'	point where light ray first enters test section
α	spatial frequency of stored holographic grid lines
β	angle of rotation of hologram
γ	apparent sensitivity
ϵ	phase parameter
θ	offset angle, angle between object and reference beams
λ_0	wavelength of illumination outside test section
Ξ,H	axes inclined at angle $\beta/2$ with respect to X'-Y' axes
ξ,η	point on moiré fringe pattern
$\Delta\xi$	fringe shift of disturbed moiré fringes
ξ_0,η_0	values of x_0', y_0' transformed to Ξ-H axis system
ρ	density of gas under flow condition
$\bar{\rho}$	average density of gas across flow region
ρ_0	density of gas under no-flow condition
$\Delta\phi$	phase-angle change corresponding to difference in optical-path length across test section
ϕ_r	phase angle of reference wave field
ϕ_r'	phase angle of reference wave field after rotation of hologram

EXPERIMENTAL CONSIDERATIONS

General Description of Apparatus and Procedure

The laboratory setup used in this holographic-interferometry technique for flow visualization is shown in figure 1. In general, the arrangement is that of a conventional holographic-recording geometry having a reference and an object beam. The separate parts of the system – including optical components, photographic plate, and supporting table – were selected and arranged under the usual constraints employed in holographic recording. The illumination source is a 50-milliwatt, 6328-Å helium-neon laser, spatially filtered via a lens-pinhole combination to produce a relatively clean, uniform output. The collimated reference and object beams, which intersect at the photographic plate, are derived from two 15-cm-diameter, f/8 mirrors. In this experiment the offset angle, the angle between the reference and object beams, is small (approximately 5^{o}), in order that the fringe pattern resulting from the interference of the two beams be relatively coarse (approximately 138 line pairs/mm). The recording of this straight-line fringe pattern results in a stored holographic grid which is used in the subsequent comparison with a real-time grid. A photomicrograph ($\times$ 450) of this stored holographic grid is shown in figure 2.

The holograms recorded during this experiment were all made using Kodak 649-F photographic plates. The photographic plates were given a standard development processing of 5 minutes in D-19, then 5 minutes in rapid fixer, and then 10 minutes in a flowing water bath at 20^{o} C (carefully controlled). Uniform temperature throughout the processing is essential.

Formation of Moiré Fringes

The flow-visualization technique reported here can be described in terms of the moiré effect, as proved in appendix A, although the grids which are used to produce the fringes are obtained holographically. The distinction is that the real-time grid is not a material grid, as with the conventional moiré effect, but is a phase grid. With this distinction, the resulting fringes in this technique can be referred to as moiré fringes.

The grids which are used in this experiment to generate the moiré fringes, in order to examine the flow phenomena in the test section of the setup, are obtained in the usual manner employed in real-time holography. The stored holographic grid is recorded on the photographic plate by intersecting the reference and object beams with no flow in the test section. The plate is removed for development processing and a positive is made. This positive is then inserted into the holographic setup at the original position which the plate occupied during the recording. When this hologram is illuminated by the reference and object beams simultaneously, each beam is reconstructed. Such illumination consti-

tutes a second grid, which is real time, from the intersection of the reference and object beams. This real-time grid is thus superposed on the stored holographic grid. To produce the moiré fringes it is necessary only to rotate the stored holographic grid (i.e., the hologram) with respect to the real-time grid. Moiré fringes, which can be used to examine flow changes in the test section, appear in real time.

Relationship of Fringe Formation to Experimental Parameters

As proved in appendix A, the moiré fringes can be observed in both the reference beam and the object beam and, for no flow in the test section, the irradiance $I_t(x',y')$ of these fringes has the following cosine dependence:

$$I_t(x',y') = 5 + 4 \cos \epsilon(x',y') \tag{1}$$

where ϵ is a phase parameter depending on the amount of hologram rotation (i.e., the angle between the two grids) and on the spatial frequency (i.e., the fringe density) of the stored holographic grid. In addition, the spatial frequency f of the undisturbed moiré fringes, as proved in appendix A from both a holographic-analysis and a conventional moiré approach, is

$$f = \frac{1}{L} = 2\alpha \sin \frac{\beta}{2} \tag{2}$$

where L is the spacing of the undisturbed moiré fringes, β is the angle of rotation of the hologram, and α is the spatial frequency of the stored holographic grid lines. This spatial frequency α is

$$\alpha = \frac{\sin \theta}{\lambda_0} \tag{3}$$

where θ is the offset angle and λ_0 is the wavelength of the illumination outside of the test section.

From equation (2), it may be noticed that the spacing of the undisturbed moiré fringes is easily adjusted by rotating the hologram. This has the effect of controlling the apparent sensitivity of the interferometer. The apparent sensitivity is discussed in detail in appendix B.

Repositioning Sensitivity

In those applications of holographic interferometry where the plate has to be repositioned accurately, various factors affect the repositioning sensitivity. One such factor is the offset angle θ. This angle determines, for example, whether the hologram is to be considered thick or thin (i.e., a volume or a plane hologram, ref. 6). The thickness can affect the repositioning sensitivity (ref. 7). Noise in the reconstruction is also affected by the offset angle (ref. 8).

In the present holographic-interferometry technique, however, these considerations are secondary compared to the relationship expressed by equation (2). In the small-angle approximation $\left(\text{i.e., when } \sin\theta = \theta, \ \sin\frac{\beta}{2} = \frac{\beta}{2}\right)$, the product of θ and β is a constant for a given desired value of the moiré spatial frequency f. This means that a small value of the offset angle θ allows a larger value of the angle of rotation β. In this technique translation errors are not particularly critical because the illuminating beams are plane waves. A sizable rotation tolerance is also desirable. A calculation using an offset angle θ of 5° and a desired moiré spatial frequency f of 0.5 line pair/mm, for example, renders the angle of rotation β equal to 14'. For a θ of 10°, this value of β would be reduced by a factor of one-half.

In addition, the physical constraints of the experimental system can also dictate the value of the offset angle θ. Small values of the offset angle require a long laboratory setup so that the two beams can separate, as can be seen from figure 1. Therefore, a compromise between repositioning tolerance and space limitations is often required.

Results

Laboratory tests were made by introducing a perturbation into one of the two real-time beams and recording the resulting moiré fringes. These moiré fringes are of good contrast and are visible throughout a large volume (out to approximately 12 ft) behind the hologram.

Figure 3 is an example of the results when the hologram is adjusted for low apparent sensitivity. Figure 3(a) shows the undisturbed moiré fringes; figure 3(b) shows the fringe shift caused by a hot soldering iron. The fringe shift varies from about three to about two fringes.

Figure 4 is an example of the results when the hologram is adjusted for high apparent sensitivity. Figure 4(a) shows the moiré fringes, undisturbed except by room thermals; figure 4(b) shows the fringe shift caused by the heat from a person's hand. The shift is only about one-half fringe.

Figure 5 is an example of the results when the hologram is adjusted such that one fringe covers the entire plate, which is known as the infinite-fringe condition, with a

lighted candle in the field. (The spiral pattern is caused by light diffracted by the shutter leaves.)

Because the stored holographic grid and the real-time grid are both transmitted through the same optical components, a permanent distortion such as in an optically poor window causes duplicate variations in the grids and, hence, straight moiré fringes. This was verified by putting a piece of commercial plate glass in one leg of the system before the stored holographic grid was made. The results are shown in figure 6. Figure 6(a) shows the undisturbed moiré fringes; figure 6(b) shows the fringe shift caused by a lighted candle. The heavy striae in the glass are visible in the readouts, as identified by the leaders; they have not, however, changed the moiré fringes.

Interpretation of Data

A brief discussion on the density determination of a gas flow from the interferometric data is given in appendix B. As pointed out in appendix B, the procedure involves determining the difference in optical-path length between two light rays, one ray traversing a region containing a flow distribution and the other ray traversing a no-flow region, shown in figure 7. The phase change $\Delta\phi(x',y')$ corresponding to the difference in optical-path length across the test section of length $\ell = \left|z_2 - z_1\right|$ is

$$\Delta\phi(x',y') = \frac{2\pi}{\lambda_0}\int_{z_1}^{z_2}\left[n(x',y',z) - n_0\left(x_0',y_0',z\right)\right]dz \tag{4}$$

where λ_0 is the wavelength of the illumination outside of the test section, $n(x',y',z)$ is the refractive index under the flow condition, and $n_0\left(x_0',y_0',z\right)$ is the refractive index under the no-flow condition.

Equation (4) can be expressed in terms of the density of the gas through the Gladstone-Dale relationship, given in appendix B. The equation relating the phase change to the density is then

$$\Delta\phi(x',y') = \frac{2\pi K}{\lambda_0}\int_{z_1}^{z_2}\left[\rho(x',y',z) - \rho_0\left(x_0',y_0',z\right)\right]dz \tag{5}$$

where K is the Gladstone-Dale constant, $\rho(x',y',z)$ is the density of the gas under the flow condition, and $\rho_0\left(x_0',y_0',z\right)$ is the density of the gas under the no-flow condition.

As proved in appendix B, the fringe shift for the finite-fringe condition is related to the corresponding density change by the following equation:

$$\frac{\Delta\xi(\xi,\eta)}{L} = \frac{K}{\lambda_0}\int_{z_1}^{z_2}\left[\rho(\xi,\eta,z) - \rho_0\left(\xi_0,\eta_0,z\right)\right]dz \tag{6}$$

where $\Delta\xi(\xi,\eta)$ is the fringe shift and L is the spacing of the undisturbed moiré fringes, shown in figure 8. The solution of equation (6), however, is not possible unless various assumptions regarding the nature of the flow are used. If plane flow (i.e., if ρ is independent of z) is assumed, equation (6) reduces to the simple form

$$\frac{\Delta\xi(\xi,\eta)}{L} = \frac{K}{\lambda_0}\left[\rho(\xi,\eta) - \rho_0\left(\xi_0,\eta_0\right)\right]\ell \tag{7}$$

If an average density $\bar{\rho}(\xi,\eta)$ across the flow region is assumed, then the quantity $\rho(\xi,\eta,z)$ may be replaced by $\bar{\rho}(\xi,\eta)$ and the corresponding form of equation (7) used.

For the infinite-fringe condition (no rotation of the hologram), the fringes for phase changes greater than or equal to 2π appear as lines of constant phase (i.e., density). Phase changes less than 2π show up only as contrast variations in the interferogram.

APPLICATION CONSIDERATIONS

The application of this holographic-interferometry technique to flow-visualization studies has three chief advantages: Real-time data for continuous observation and photography, ease of optical adjustment, and capability of using ordinary-glass test-section windows without affecting the results.

Certain problems, however, which are inherent in more conventional flow-visualization methods also appear in the present technique. For example, the usual constraints which are encountered in a facility environment, such as vibrations and room thermals, affect this holographic-interferometry technique in the same manner as in a sensitive schlieren system.

Further, in applying this system to wind-tunnel experiments, difficulties may be encountered due to obstructions in the leg of the system that bypasses the tunnel test section. One method which can be employed to circumvent any physical constraints imposed by the wind tunnel is to use a system such as that shown in figure 9, which is similar to a Mach-Zehnder interferometer. If this is done, however, the beam splitters which are used in the interferometer must have sufficient wedging between the front and back surfaces so that the interference effects due to the internal reflections can be eliminated. A system using beam splitters without sufficient wedging has been tried in the laboratory; and, even though the surfaces were antireflective coated, the result was that severe

degradation of the data occurred due to the spurious interference effects from the front and back surfaces. An alternative to using wedge plates may be pellicles; however, unwanted effects can be produced by the vibration of the pellicles. If the obstructions to the optical system are not large, a system similar to that shown in figure 1 may be used.

The moiré fringes appear in both beams of the system and can be photographed after the beams have separated. In this experiment 16-mm motion pictures were also taken of the results; they were taken at 24 frames/sec on High-Speed Ektachrome by directly photographing a screen. The still photographs in figures 3 to 6 were taken by refocusing the 15-cm-diameter beam to a point image by a spherical mirror, shown in figure 1. Refocusing the light to a point image, which is a standard procedure in most schlieren systems, allows a small-diameter lens to accommodate the entire beam without vignetting the image.

Some final comments on application procedures include: (1) All components must be mounted upon the same structure, which must be relatively rigid; (2) the mirror adjustments, which are necessary for recovering the fringes if the system is changed, must be precise and must work smoothly; and (3) the plate holder must have precision adjustments, which are necessary for adjusting the moiré fringe spacing to the desired apparent sensitivity, rotationally in the plane of the hologram.

The technique described in this paper, with a setup similar to that of figure 1, is presently being successfully applied to study the flow in the Langley pilot model expansion tube. A high-speed film drum, moving with a speed of 5080 cm/sec, and a 0.01524-cm slit are used in conjunction with the system to obtain time-resolved interferograms. The exposure used is hence 3 μsec.

CONCLUDING REMARKS

A relatively simple holographic-interferometry technique for flow visualization and analysis has been described from both experimental and application considerations. This technique produces good-contrast moiré fringes, which are visible throughout a large volume behind the hologram. The readout may be continuously observed or photographed in real time. The system is easy to adjust and is not affected by optically poor windows enclosing the test section. This holographic-interferometry technique offers a simplified and accurate means to measure flow characteristics interferometrically.

Langley Research Center,
National Aeronautics and Space Administration,
Hampton, Va., November 22, 1973.

APPENDIX A

COMPARISON OF HOLOGRAPHIC AND MOIRÉ FRINGES

Recording the Hologram

The formation of the stored holographic grid with the setup shown in figure 1 can be analyzed with the aid of figure 10. In this setup the object beam is perpendicularly incident on the photographic plate. For plane-wave reference and object beams offset at an angle θ in the Y-Z plane, the amplitude A(y) incident on the recording plane is

$$A(y) = A_r \exp\left[-i\phi_r(y)\right] + A_o \tag{A1}$$

where A_r is the amplitude of the reference wave field, $\phi_r(y)$ is the phase of the reference wave field, and A_o is the amplitude of the object wave field. The phase $\phi_r(y)$ is

$$\phi_r(y) = 2\pi y\alpha \tag{A2}$$

where α is the spatial frequency of the stored holographic grid lines, due to the offset angle θ, and is

$$\alpha = \frac{\sin\theta}{\lambda_0} \tag{A3}$$

where λ_0 is the wavelength of the illumination outside of the test section.

This geometry thus generates a set of straight-line fringes having a cosine irradiance distribution I(y) as follows:

$$\begin{aligned} I(y) &= \left|A(y)\right|^2 \\ &= \left\{A_r \exp\left[-i\phi_r(y)\right] + A_o\right\}\left\{A_r \exp\left[i\phi_r(y)\right] + A_o\right\} \\ &= {A_r}^2 + {A_o}^2 + A_rA_o\left\{\exp\left[-i\phi_r(y)\right] + \exp\left[i\phi_r(y)\right]\right\} \\ &= {A_r}^2 + {A_o}^2 + 2A_rA_o\cos\phi_r(y) \end{aligned} \tag{A4}$$

Reconstruction

The positive hologram, after processing, is inserted into the holographic setup at the original position of the photographic plate (i.e., the recording plane) and is illuminated simultaneously by the reference beam and the object beam. The resulting reconstructed (i.e., transmitted) amplitude $A_t(y)$ (if the operation is in the linear region of the transmission-exposure curve of the photographic plate) is

$$A_t(y) \propto \left\{A_r \exp\left[-i\phi_r(y)\right] + A_o\right\}\left(A_r^2 + A_o^2 + A_rA_o\left\{\exp\left[-i\phi_r(y)\right] + \exp\left[i\phi_r(y)\right]\right\}\right)$$

Or,

$$A_t(y) \propto A_o\left(2A_r^2 + A_o^2\right) + A_r\left(2A_o^2 + A_r^2\right)\exp\left[-i\phi_r(y)\right] + A_rA_o^2\exp\left[i\phi_r(y)\right]$$

$$+ A_oA_r^2\exp\left\{-i\left[2\phi_r(y)\right]\right\} \tag{A5}$$

Expression (A5) is for the hologram replaced in its original position with no rotation. Now the form of the reconstructed amplitude after the hologram is rotated must be determined.

Reconstruction After Rotation of Hologram; No Flow in Object Beam

The geometry for the rotated hologram is shown in figure 11. The unprimed coordinates are fixed on the hologram and thus rotate with it. The primed coordinates represent the recording plane during the reconstruction. Thus, it can be seen that in the unprimed system a set of fringes (i.e., a grid), given by equation (A4), is present.

In this holographic-interferometry technique, the hologram is illuminated simultaneously by the reference beam and the object beam. The resulting reconstructed amplitude $A_t'(x',y')$ for the rotated hologram with no flow in the object beam is

$$A_t'(x',y') \propto \left\{A_r \exp\left[-i\phi_r'(y')\right] + A_o\right\}\left(A_r^2 + A_o^2 + A_rA_o\left\{\exp\left[-i\phi_r(x',y')\right] + \exp\left[i\phi_r(x',y')\right]\right\}\right)$$

Or,

$$A_t'(x',y') \propto C_2A_O \exp\left\{-i\left[\phi_r'(y') + \phi_r(x',y')\right]\right\} + C_1A_r \exp\left[-i\phi_r'(y')\right]$$

$$+ C_3A_r \exp\left[-i\phi_r(x',y')\right] + C_2A_O \exp\left\{-i\left[\phi_r'(y') - \phi_r(x',y')\right]\right\} + C_1A_O$$

$$+ C_3A_r \exp\left[i\phi_r(x',y')\right] \tag{A6}$$

where

$$C_1 = A_r^2 + A_O^2 \tag{A7}$$

$$C_2 = A_r^2 \tag{A8}$$

$$C_3 = A_O^2 \tag{A9}$$

$$\phi_r'(y') = 2\pi y'\alpha \tag{A10}$$

and

$$\phi_r(x',y') = 2\pi\alpha(y' \cos\beta - x' \sin\beta) \tag{A11}$$

The phase $\phi_r'(y')$ is the phase of the reference wave field after the rotation of the hologram. The phase $\phi_r(x',y')$ is the phase of the reference wave field before the rotation of the hologram, in terms of the primed coordinates, where β is the angle through which the hologram is rotated.

Further, a phase parameter $\epsilon(x',y')$ can be defined as

$$\epsilon(x',y') = \phi_r'(y') - \phi_r(x',y') \tag{A12}$$

Substituting equations (A10) and (A11) into equation (A12) yields

$$\epsilon(x',y') = 2\pi\alpha\left[x' \sin\beta + y'(1 - \cos\beta)\right] \tag{A13}$$

Eliminating $\phi_r(x',y')$ between expressions (A6) and (A13) yields for the reconstructed amplitude $A_t'(x',y')$ for the rotated hologram with no flow in the object beam

$$A_t'(x',y') \propto \underbrace{C_2A_o \exp\left\{-i\left[2\phi_r'(y') - \epsilon(x',y')\right]\right\}}_{1} + \underbrace{C_1A_r \exp\left[-i\phi_r'(y')\right]}_{2}$$

$$+ \underbrace{C_3A_r \exp\left\{-i\left[\phi_r'(y') - \epsilon(x',y')\right]\right\}}_{3} + \underbrace{C_2A_o \exp\left[-i\epsilon(x',y')\right]}_{4} + \underbrace{C_1A_o}_{5}$$

$$+ \underbrace{C_3A_r \exp\left\{i\left[\phi_r'(y') - \epsilon(x',y')\right]\right\}}_{6} \tag{A14}$$

If in term 4 of expression (A14)

$$\frac{k_{X'}}{k_Z} << 1 \tag{A15}$$

and

$$\frac{k_{Y'}}{k_Z} << 1 \tag{A16}$$

where $k_{X'}$, $k_{Y'}$, and k_Z are the propagation numbers associated with the X', Y', and Z directions, respectively, then the reconstructed object beam can be regarded as a combination of terms 4 and 5. Now,

$$\frac{k_{X'}}{k_Z} = \frac{\frac{\partial \epsilon}{\partial x'}}{\frac{2\pi}{\lambda_0}}$$

Using equation (A13) gives

$$\frac{k_{X'}}{k_Z} = \frac{\frac{2\pi}{\lambda_0} \sin\theta \sin\beta}{\frac{2\pi}{\lambda_0}}$$

For small angles

$$\frac{k_{X'}}{k_Z} = \theta\beta \tag{A17}$$

Also,

$$\frac{k_{Y'}}{k_Z} = \frac{\frac{\partial \epsilon}{\partial y'}}{\frac{2\pi}{\lambda_0}}$$

Using equation (A13) gives

$$\frac{k_{Y'}}{k_Z} = \frac{\frac{2\pi}{\lambda_0} \sin\theta(1 - \cos\beta)}{\frac{2\pi}{\lambda_0}}$$

For small angles

$$\frac{k_{Y'}}{k_Z} = \theta\beta^2 \tag{A18}$$

Hence, expressions (A15) to (A18) render

$$\theta\beta << 1 \tag{A19}$$

as the condition which must be satisfied in order to regard the reconstructed object beam as a combination of terms 4 and 5. If the Z-axis is rotated so that it is alined with the initial direction of the reference beam, instead of the object beam, then a similar analysis for term 3 of expression (A14) produces expression (A19) as the condition which must be satisfied in order to regard the reconstructed reference beam as a combination of terms 2 and 3. Therefore, if expression (A19) is satisfied, then the reconstructed amplitude $A_t'(x',y')$ can be regarded as being composed of four, instead of six, different reconstructed wave fronts separated in space. Terms 1, 2 plus 3, 4 plus 5, and 6 of expression (A14) each give one of these four reconstructed wave fronts. The six terms of expression (A14) are shown in figure 12.

It may be noticed that neither the irradiance of term 1 nor the irradiance of term 6 gives fringes. It may also be noted that the irradiance of terms 2 plus 3 and the irradiance of terms 4 plus 5 give fringes in the reference and object beams, respectively. In the reference beam the amplitude is

$$A_r\left\{C_1 + C_3 \exp\left[i\epsilon(x',y')\right]\right\}\exp\left[-i\phi_r'(y')\right]$$

and in the object beam the amplitude is

$$A_o\left\{C_1 + C_2 \exp\left[-i\epsilon(x',y')\right]\right\}$$

If, for simplicity, it is assumed that $A_r = A_o = 1$, then the observed irradiance $I_t(x',y')$ of the fringes appearing in both the reference and object beams under the no-flow condition is

$$I_t(x',y') = \left|\left\{2 + \exp\left[i\epsilon(x',y')\right]\right\}\exp\left[-i\phi_r'(y')\right]\right|^2$$

$$= \left|2 + \exp\left[-i\epsilon(x',y')\right]\right|^2$$

$$= 5 + 4\cos\epsilon(x',y') \qquad \text{(A20)}$$

Thus, for no flow in the object beam, the superposition of the stored holographic grid and the real-time grid results in a set of cosine fringes that are observable in either the reference beam or the object beam.

Spatial Frequency of Fringes; From Holographic Analysis

The spatial frequency of the fringes which appear in both the reference and object beams under the no-flow condition is determined by examining the irradiance $I_t(x',y')$ of the fringes, given by equation (A20). Substituting equation (A13) into equation (A20) furnishes

$$I_t(x',y') = 5 + 4 \cos\left\{2\pi\alpha\left[x' \sin\beta + y'(1 - \cos\beta)\right]\right\} \tag{A21}$$

Comparing equation (A21) to the general form

$$I_t(x',y') = 5 + 4 \cos\left[2\pi\left(x'f_{X'} + y'f_{Y'}\right)\right] \tag{A22}$$

where $f_{X'}$ and $f_{Y'}$ are the X'- and Y'-components of the spatial frequency f, respectively, gives

$$f_{X'} = \alpha \sin\beta = \frac{\sin\theta}{\lambda_0} \sin\beta \tag{A23}$$

$$f_{Y'} = \alpha(1 - \cos\beta) = \frac{\sin\theta}{\lambda_0}(1 - \cos\beta) \tag{A24}$$

From figure 13 and equations (A23) and (A24), it is seen that the spatial frequency f and the spacing L of the dark (or bright) fringes are given by

$$f = \frac{1}{L} = 2\alpha \sin\frac{\beta}{2} = 2\frac{\sin\theta}{\lambda_0} \sin\frac{\beta}{2} \tag{A25}$$

The fringes are oriented such that they make an angle $\beta/2$ with respect to the X'-axis, shown in figure 13. In this experiment the angle β through which the hologram is rotated is approximately 1^o; hence, the angle $\beta/2$ is approximately 30'. Therefore, the fringes are nearly parallel to the Y'-axis.

Equation (A25) shows that the spatial frequency f of the fringes is easily changed by varying the angle of rotation β. This is shown in figure 14, where the spatial frequency f is plotted against the angle of rotation β for a fixed value of $\alpha = \frac{\sin\theta}{\lambda_0}$. For the values of $\theta = 5^o$ and $\lambda_0 = 6328$ Å, which are the values used in this experiment, the spatial frequency of the resulting fringe pattern is slightly larger than 2 line pairs/mm.

Spatial Frequency of Fringes; From Conventional Moiré Approach

The previous results, specifically equation (A25), can also be obtained by the geometrical methods that are employed in conventional moiré techniques (ref. 9). Moiré

fringes are generally formed by the superposition of material grids; and the derivation of the resulting fringe pattern is straightforward, especially for the superposition of two straight-line grids.

From figure 15,

$$c^2 = a^2 + b^2 - 2ab \cos \beta \tag{A26}$$

where β is the angle of rotation of the hologram. Also, from figure 15, it may be seen that the area of BCED is given by

$$BCED = cL = ae = bd \tag{A27}$$

where L is the spacing of the moiré fringes, e is the spacing of the real-time grid lines, and d is the spacing of the stored holographic grid lines. Using equations (A26) and (A27) yields

$$\frac{1}{L^2} = \frac{1}{e^2} + \frac{1}{d^2} - \frac{2}{ed} \cos \beta \tag{A28}$$

When d and e are assumed equal,

$$\frac{1}{L^2} = \frac{2}{d^2}(1 - \cos \beta) \tag{A29}$$

Since $d = 1/\alpha$, with use of trigonometric identities, equation (A29) reduces to

$$f = \frac{1}{L} = 2\alpha \sin \frac{\beta}{2} \tag{A30}$$

which is identical to equation (A25) derived earlier by using a holographic analysis. Thus, it is proved that this technique, although indeed holographic, can be equivalently visualized in terms of the conventional moiré effect.

APPENDIX B

DENSITY DETERMINATION FROM HOLOGRAM

Phase Change

The determination of density changes in a flow field from an interferogram is well-known (ref. 10). However, a brief treatment is given here in order to show how the holographic results apply.

A flow region of refractive index $n(x',y',z)$ through which a light ray propagates is shown in figure 7. (The primed coordinates are used in order to be consistent with the convention adopted in appendix A.) Initially, for an undeflected ray propagating parallel to the Z-axis through a no-flow region of refractive index n_0, the optical-path length O_1 across the test section of length $\ell = |z_2 - z_1|$ is

$$O_1 = \int_{z_1}^{z_2} n_0\left(x_0',y_0',z\right)dz \tag{B1}$$

where $\left(x_0',y_0'\right)$ is the point at which the light ray first enters the test section. For a deflected light ray in the flow region of refractive index n, the optical-path length O_2 is

$$O_2 = \int_{z_1}^{z_2} n(x',y',z)ds \tag{B2}$$

where ds is the differential arc length, shown in figure 7, for the deflected ray. If the deflections are small, then the changes in the optical-path length are only small numbers of wavelengths. This is a condition that is satisfied in flow problems; hence, ds in equation (B2) is approximately equal to and can be replaced by dz.

The difference in optical-path length is then

$$O_2 - O_1 = \int_{z_1}^{z_2} \left[n(x',y',z) - n_0\left(x_0',y_0',z\right)\right]dz \tag{B3}$$

The amount of phase change $\Delta\phi(x',y')$ between the flow and no-flow conditions is thus

$$\Delta\phi(x',y') = \frac{2\pi}{\lambda_0}\int_{z_1}^{z_2} \left[n(x',y',z) - n_0\left(x_0',y_0',z\right)\right]dz \tag{B4}$$

where λ_0 is the wavelength of the illumination outside of the test section.

In most flow problems the refractive index of the gas can be related to the density through the Gladstone-Dale relationship (ref. 11)

$$n = 1 + K\rho \tag{B5}$$

where K is the Gladstone-Dale constant, which depends on the gas and the wavelength, and where ρ is the density of the gas in the flow region. Thus, equation (B4) becomes

$$\Delta\phi(x',y') = \frac{2\pi K}{\lambda_0}\int_{z_1}^{z_2}\left[\rho(x',y',z) - \rho_0\left(x_0',y_0',z\right)\right]dz \tag{B6}$$

where $\rho_0\left(x_0',y_0',z\right)$ is the density of the gas in the no-flow region.

The integral in equation (B6) can be evaluated for certain types of flow, for example, plane flow. For the problem of plane flow (i.e., when ρ is independent of z), equation (B6) reduces to

$$\Delta\phi(x',y') = \frac{2\pi K}{\lambda_0}\left[\rho(x',y') - \rho_0\left(x_0',y_0'\right)\right]\ell \tag{B7}$$

If plane flow does not exist, then the quantity $\rho(x',y',z)$ may be replaced by an average density $\bar{\rho}(x',y')$ across the flow region and the corresponding form of equation (B7) used.

Finite-Fringe Condition

With an interferometer, either conventional (e.g., Mach-Zehnder) or holographic, either finite-fringe or infinite-fringe interferograms can be generated. The finite-fringe condition is obtained when the beam corresponding to the flow condition (e.g., real-time object beam with flow) and the beam corresponding to the no-flow condition (e.g., reconstructed object beam) intersect at a small angle. A set of background fringes is thus generated, and a small phase change in the object beam due to the flow is observed as a shift in these background fringes.

A convenient method for generating this background-fringe set in holographic interferometry is to rotate the hologram, which is the method that is used in the technique reported in this paper. The spacing of these moiré fringes (and, hence, the apparent sensitivity, as is shown) is easily adjusted through the angle of rotation β, as discussed in appendix A.

When a flow is introduced into the object beam, the object beam then takes on the form $\exp\left[-i\,\Delta\phi(x',y')\right]$, where $\Delta\phi(x',y')$ is the phase change between the flow and

no-flow conditions at a point (x',y') on the hologram. If the hologram is illuminated by the reference beam and the object beam simultaneously, then the reconstructed amplitude for the rotated hologram with a flow in the object beam is

$$A_t'(x',y') \propto \left\{A_r \exp\left[-i\phi_r'(y')\right] + A_o \exp\left[-i\,\Delta\phi(x',y')\right]\right\}\left(A_r^2 + A_o^2 + A_rA_o\left\{\exp\left[-i\phi_r(x',y')\right] + \exp\left[i\phi_r(x',y')\right]\right\}\right)$$

Or,

$$A_t'(x',y') \propto \underbrace{C_2A_o \exp\left\{-i\left[2\phi_r'(y') - \epsilon(x',y')\right]\right\}}_{1} + \underbrace{C_1A_r \exp\left[-i\phi_r'(y')\right]}_{2}$$

$$+ \underbrace{C_3A_r \exp\left\{-i\left[\phi_r'(y') + \Delta\phi(x',y') - \epsilon(x',y')\right]\right\}}_{3} + \underbrace{C_2A_o \exp\left[-i\epsilon(x',y')\right]}_{4}$$

$$+ \underbrace{C_1A_o \exp\left[-i\,\Delta\phi(x',y')\right]}_{5} + \underbrace{C_3A_r \exp\left\{i\left[\phi_r'(y') - \Delta\phi(x',y') - \epsilon(x',y')\right]\right\}}_{6} \qquad \text{(B8)}$$

where the phase parameter $\epsilon(x',y')$ is given by equation (A12) and where the parameters C_1, C_2, and C_3 are given by equations (A7), (A8), and (A9), respectively. Expression (B8) is analogous to expression (A14), which is for the no-flow condition.

As was pointed out in appendix A, the interference of terms 2 plus 3 and the interference of terms 4 plus 5 on the right-hand side of expression (B8) give moiré fringes in the reference and object beams, respectively. In the object beam the amplitude is

$$A_o\left\{C_1 \exp\left[-i\,\Delta\phi(x',y')\right] + C_2 \exp\left[-i\epsilon(x',y')\right]\right\}$$

If $A_r = A_o = 1$, this amplitude becomes

$$2 \exp\left[-i\ \Delta\phi(x',y')\right] + \exp\left[-i\epsilon(x',y')\right]$$

Hence, the irradiance $I_o(x',y')$ of the moiré fringes appearing in the object beam under the flow condition is

$$I_o(x',y') = \left|2 \exp\left[-i\ \Delta\phi(x',y')\right] + \exp\left[-i\epsilon(x',y')\right]\right|^2$$

$$= 5 + 4 \cos\left[\epsilon(x',y') - \Delta\phi(x',y')\right] \tag{B9}$$

The undisturbed moiré fringes (i.e., when $\Delta\phi(x',y') = 0$) make an angle $\beta/2$ with respect to the X'-axis, as discussed in appendix A. For convenience, the axis system can be transformed to a system of axes Ξ-H that is inclined at an angle $\beta/2$ with respect to the X'-Y' axes. These new axes are shown in figure 7. The equations of transformation expressing x' and y' in terms of ξ and η are

$$x' = \xi \cos\frac{\beta}{2} - \eta \sin\frac{\beta}{2} \tag{B10}$$

$$y' = \xi \sin\frac{\beta}{2} + \eta \cos\frac{\beta}{2} \tag{B11}$$

where β is the angle of rotation of the hologram. Substituting equations (B10) and (B11) into equation (A13) and using trigonometric identities produce the following expression for the phase parameter ϵ in terms of the new coordinates:

$$\epsilon(\xi) = 4\pi\alpha\xi \sin\frac{\beta}{2} \tag{B12}$$

where α is the spatial frequency of the stored holographic grid lines. In terms of these coordinates ξ and η and with the use of equation (B12) for $\epsilon(\xi)$, equation (B9) becomes

$$I_0(\xi,\eta) = 5 + 4\cos\left[4\pi\alpha\xi \sin\frac{\beta}{2} - \Delta\phi(\xi,\eta)\right] \tag{B13}$$

From equation (B13), it may be noticed that a phase change $\Delta\phi(\xi,\eta)$ results in a shifting of the fringe pattern along the Ξ-axis (i.e., disturbed fringes), shown in figure 8. The minima of this fringe pattern appear wherever

$$\Delta\phi(\xi) = 4\pi\alpha\xi \sin\frac{\beta}{2} - (2m \cdot 1)\pi \tag{B14}$$

where $m = 1, 2, 3, \ldots$.

Equation (B13) can be rewritten as

$$I_0(\xi,\eta) = 5 + 4\cos\left[\frac{2\pi}{L}\xi - \Delta\phi(\xi,\eta)\right] \tag{B15}$$

by using from equation (A25) $\frac{1}{L} = 2\alpha \sin\frac{\beta}{2}$, where L is the spacing of the undisturbed moiré fringes. A sketch of the moiré fringes described by equation (B14) and their resulting shift is shown in figure 8. It may be noted that the fringe shift $\Delta\xi$ measured along the Ξ-axis can be related to the corresponding phase change $\Delta\phi$ by

$$\Delta\xi = \frac{L}{2\pi}\Delta\phi \tag{B16}$$

Equation (B16) thus defines an apparent sensitivity γ as

$$\gamma = \frac{\Delta\xi}{\Delta\phi} = \frac{L}{2\pi}$$

Again, with use of equation (A25),

$$\gamma = \frac{\lambda_0}{4\pi \sin\theta \sin\frac{\beta}{2}} \tag{B17}$$

In the small-angle approximation $\left(\text{i.e., when } \sin\theta = \theta, \ \sin\frac{\beta}{2} = \frac{\beta}{2}\right)$, the apparent sensitivity γ becomes

$$\gamma = \frac{\lambda_0}{2\pi\theta\beta} \tag{B18}$$

By using equations (B16) and (B6), the relationship between the fringe shift $\Delta\xi$ and the density for the finite-fringe condition is proved to be

$$\frac{\Delta\xi(\xi,\eta)}{L} = \frac{K}{\lambda_0}\int_{z_1}^{z_2}\left[\rho(\xi,\eta,z) - \rho_0\left(\xi_0,\eta_0,z\right)\right]dz \tag{B19}$$

As discussed previously, if plane flow is assumed, equation (B19) takes on the form

$$\frac{\Delta\xi(\xi,\eta)}{L} = \frac{K}{\lambda_0}\left[\rho(\xi,\eta) - \rho_0\left(\xi_0,\eta_0\right)\right]\ell \tag{B20}$$

If an average density $\bar{\rho}(\xi,\eta)$ across the flow region is assumed, then the quantity $\rho(\xi,\eta,z)$ may be replaced by $\bar{\rho}(\xi,\eta)$ and the corresponding form of equation (B20) used.

It may be noticed that, for the finite-fringe condition, phase changes less than 2π can be easily measured in terms of the fringe shift $\Delta\xi$. In addition, the moiré fringe spacing and, hence, the apparent sensitivity as indicated by equation (B17) or equation (B18) can be controlled by the angle of rotation β. Further, since the density changes are determined by measuring the shift in the fringe position, a proper orientation of the flow with respect to the moiré fringes is necessary in order to maintain a reference point (i.e., parts of the fringe pattern should remain stationary, as was the situation for the display of fig. 6).

Infinite-Fringe Condition

The infinite-fringe condition is obtained when the beam corresponding to the flow condition (e.g., real-time object beam with flow) and the beam corresponding to the no-flow condition (e.g., reconstructed object beam) do not intersect at an angle. In this holographic-interferometry technique this condition is obtained when the hologram is not rotated (i.e., when $\beta = 0$). By letting $\beta \to 0$ in equation (B13) or equivalently letting $L \to \infty$ in equation (B15), it may be proved that the irradiance I_0 of the fringes appearing in the object beam under the flow condition for infinite-fringe interferometry is

$$I_0 = 5 + 4 \cos \Delta\phi \tag{B21}$$

The minima of this fringe pattern for the infinite-fringe condition appear wherever

$$\Delta\phi = (2m - 1)\pi \tag{B22}$$

where $m = 1, 2, 3, \ldots$. From equation (B22), it may be noticed that a dark fringe appears wherever

$$\Delta\phi = (2m - 1)\pi = \frac{2\pi K}{\lambda_0} \int_{z_1}^{z_2} \left(\rho - \rho_0\right) dz \tag{B23}$$

or wherever the difference in optical-path length is

$$(2m - 1)\frac{\lambda_0}{2} = K \int_{z_1}^{z_2} \left(\rho - \rho_0\right) dz \tag{B24}$$

By letting $\beta \rightarrow 0$ in equation (B17) or equation (B18), it may be established that the apparent sensitivity for the infinite-fringe condition is infinite. The fringes for phase changes greater than or equal to 2π are lines of constant phase (i.e., density). For phase changes less than 2π, fringes do not appear; such phase changes show up only as shades of brightness in the interferogram, as is evident from equation (B21).

REFERENCES

1. Heflinger, L. O.; Wuerker, R. F.; and Brooks, R. E.: Holographic Interferometry. J. Appl. Phys., vol. 37, no. 2, Feb. 1966, pp. 642-649.

2. Chau, Henry H. M.; and Mullaney, George J.: Holographic Moiré Patterns; Their Application to Flow Visualization in Aerodynamics. Appl. Opt., vol. 6, no. 8, Aug. 1967, pp. 1428-1430.

3. Tanner, L. H.: Some Applications of Holography in Fluid Mechanics. J. Sci. Instrum., vol. 43, no. 2, Feb. 1966, pp. 81-83.

4. Brooks, R. E.; Heflinger, L. O.; and Wuerker, R. F.: Interferometry With a Holographically Reconstructed Comparison Beam. Appl. Phys. Lett., vol. 7, no. 9, Nov. 1, 1965, pp. 248-249.

5. Spencer, Robert C.; and Anthony, Sheila A. T.: Real-Time Holographic Moiré Patterns for Flow Visualization. Appl. Opt., vol. 7, no. 3, Mar. 1968, p. 561.

6. Goodman, Joseph W.: An Introduction to the Principles and Applications of Holography. Proc. IEEE, vol. 59, no. 9, Sept. 1971, pp. 1292-1304.

7. Smith, Howard M.: Principles of Holography. Wiley—Interscience, c.1969, Chapter 4.

8. Goodman, Joseph W.: Introduction to Fourier Optics. McGraw-Hill Book Co., Inc., c.1968, Chapter 8.

9. Nishijima, Yasunori; and Oster, Gerald: Moiré Patterns: Their Application to Refractive Index and Refractive Index Gradient Measurements. J. Opt. Soc. Amer., vol. 54, no. 1, Jan. 1964, pp. 1-5.

10. Schardin, H.: Theory and Applications of the Mach-Zehnder Interference-Refractometer. Univ. Texas, Defense Res. Lab., 1946.

11. Cambel, Ali Bulent; and Jennings, Burgess H.: Gas Dynamics. McGraw-Hill Book Co., Inc., 1958.

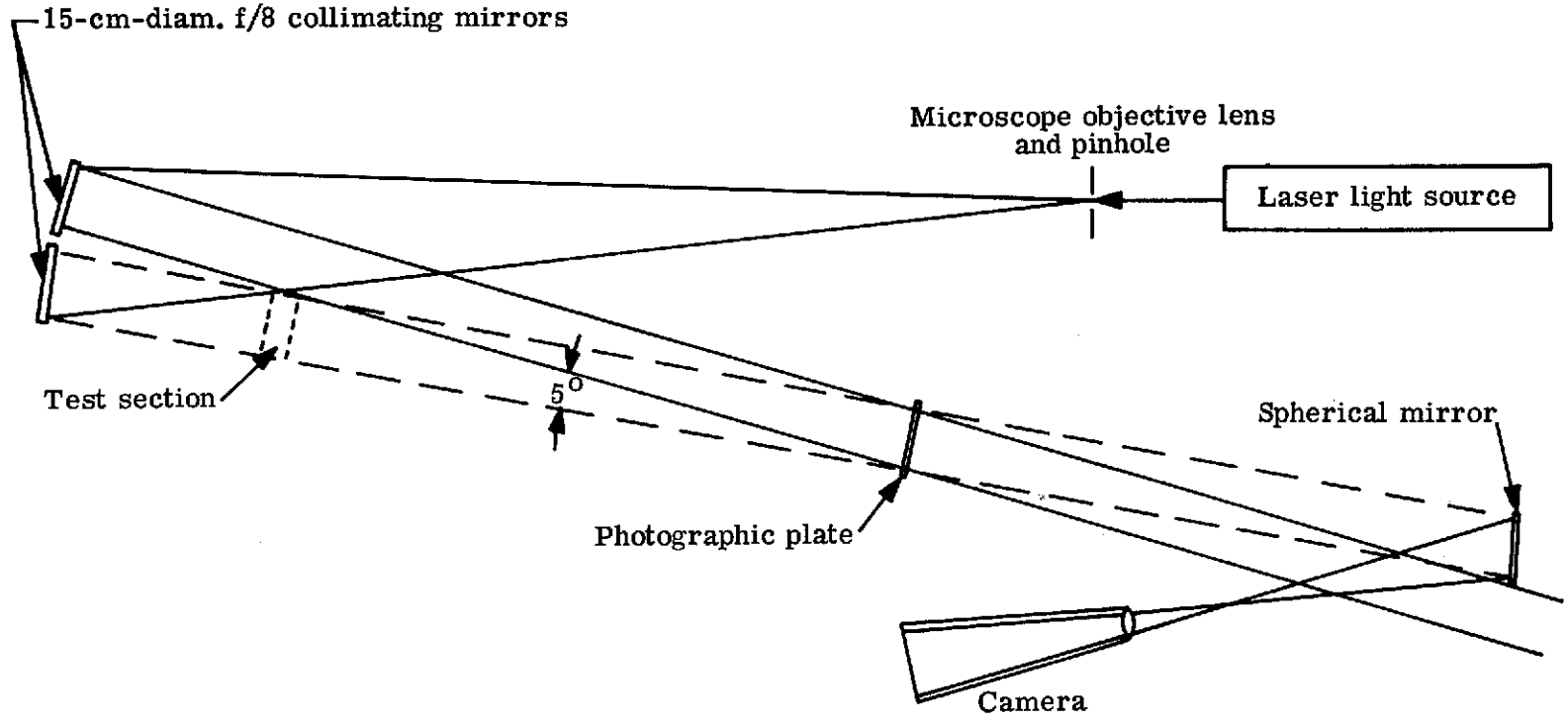

Figure 1.- Laboratory setup for holographic-interferometry technique.

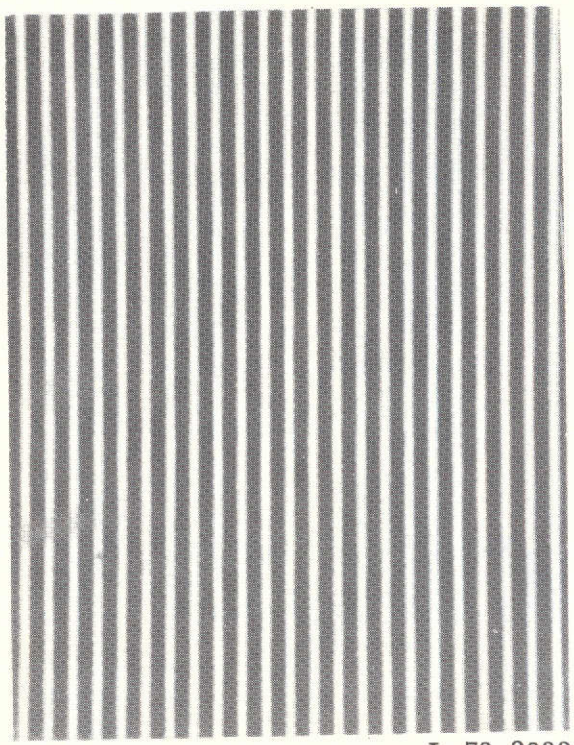

L-73-8033

Figure 2.- Photomicrograph (× 450) of stored holographic grid.

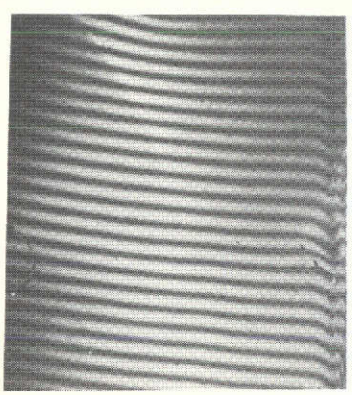

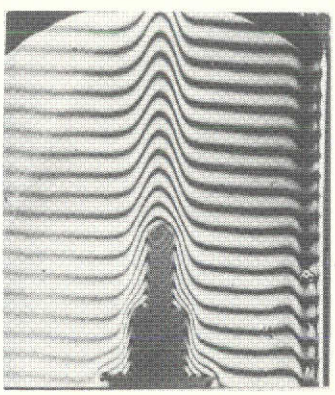

L-73-8034

(a) Undisturbed fringes.

(b) Fringe shift caused by hot soldering iron.

Figure 3.- Fringe patterns at low apparent sensitivity.

(a) Fringes, undisturbed except by room thermals.

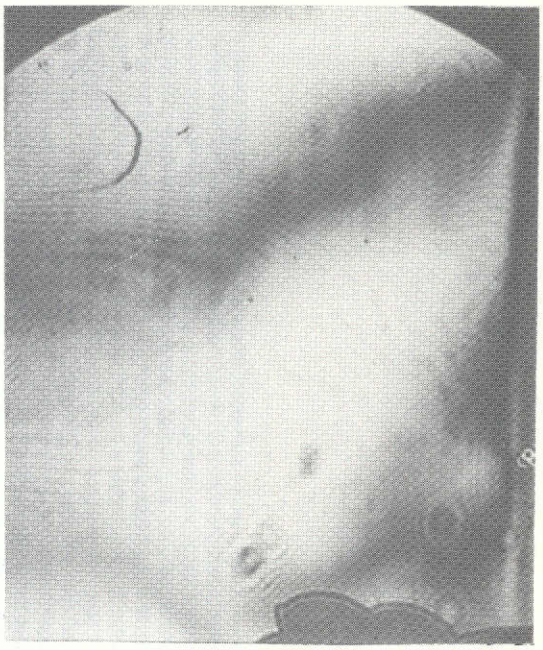

L-73-8035

(b) Fringe shift caused by heat from a person's hand.

Figure 4.- Fringe patterns at high apparent sensitivity.

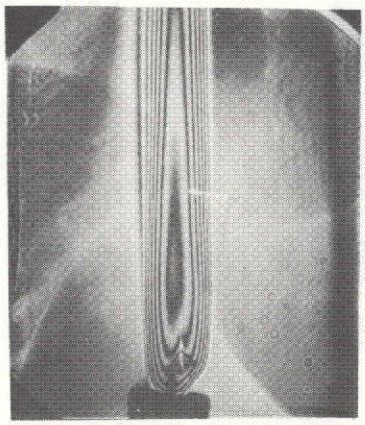

L-73-8036

Figure 5.- Fringe pattern with system adjusted for infinite-fringe condition with lighted candle in field.

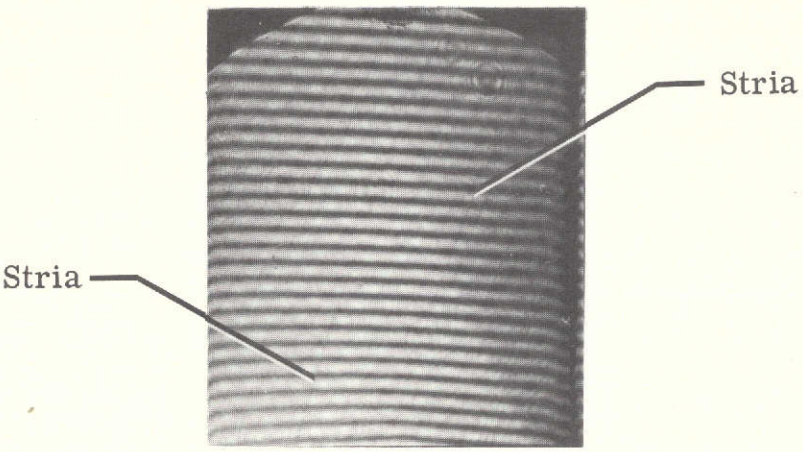

(a) Undisturbed fringes.

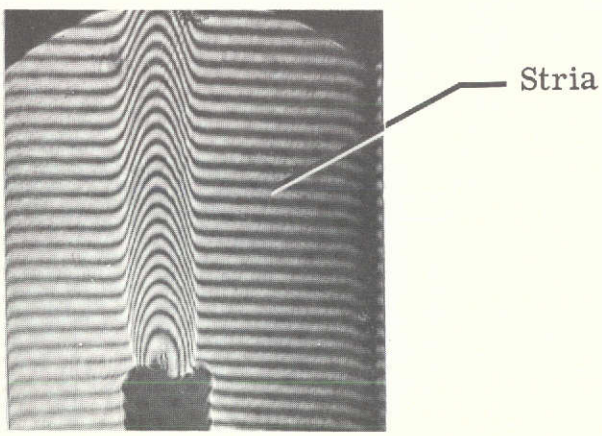

L-73-8037

(b) Fringe shift caused by lighted candle.

Figure 6.- Fringe patterns with commercial plate glass in field.

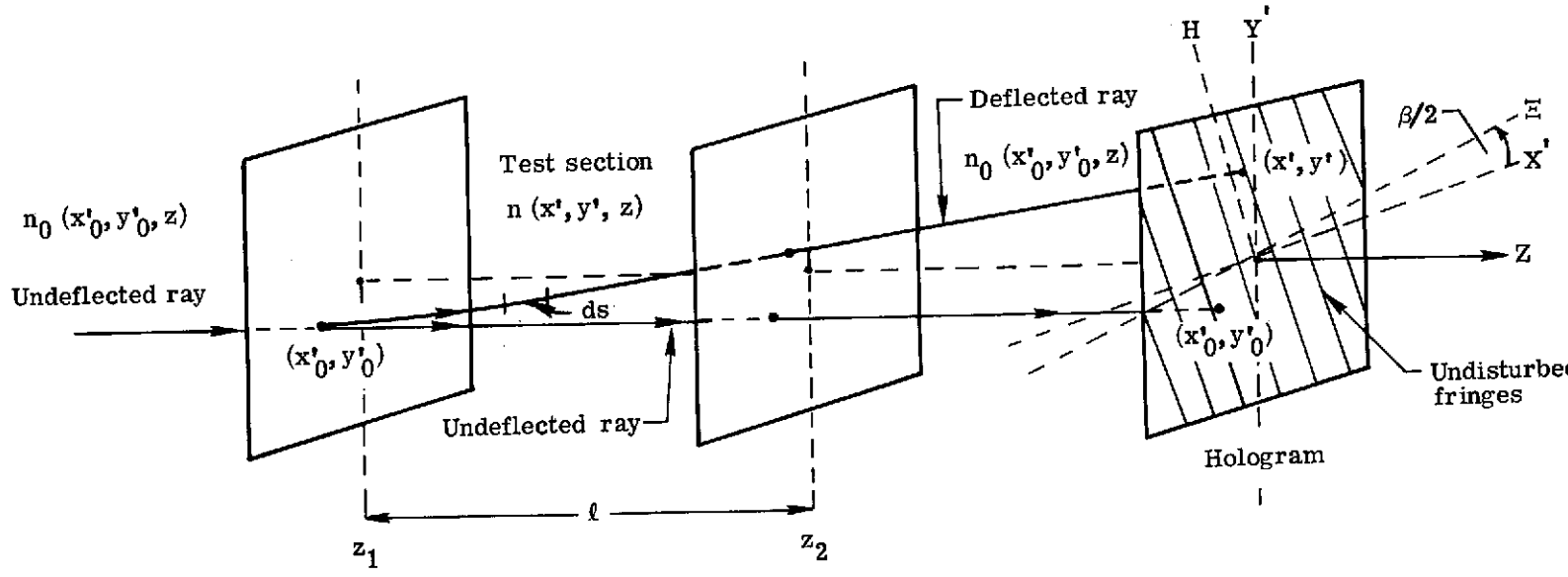

Figure 7.- Deflection of light ray through medium having refractive-index gradient.

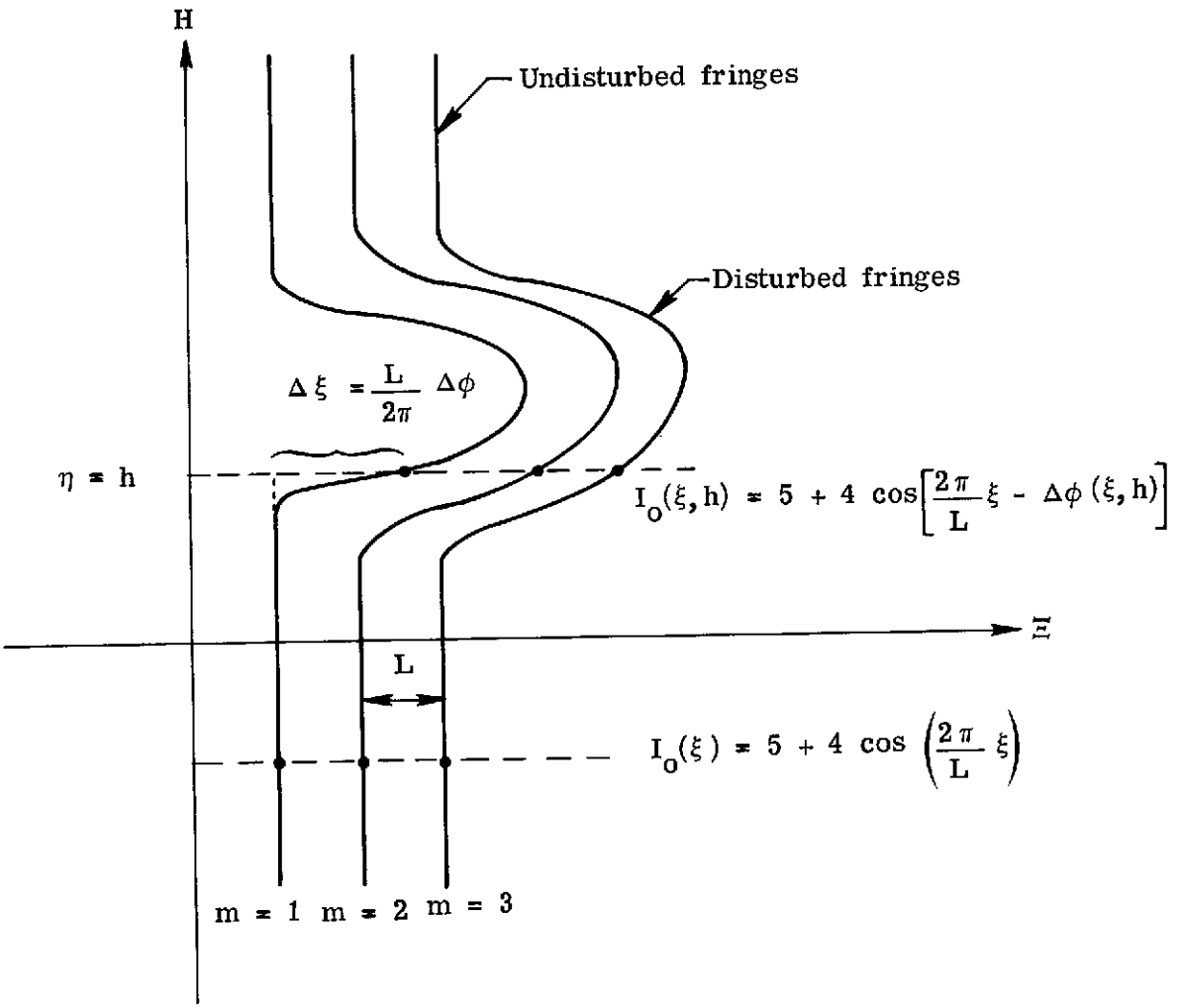

Figure 8.- Shift of fringe pattern due to phase change.

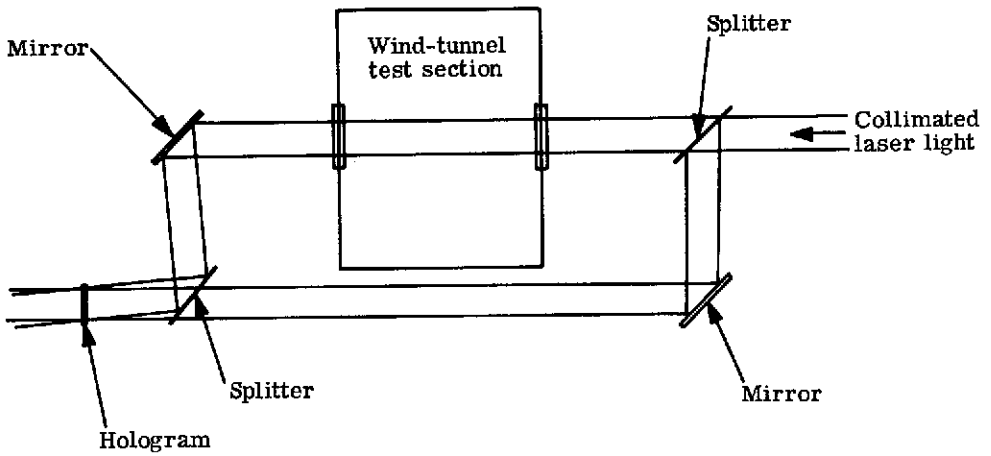

Figure 9.- Holographic-interferometry technique applied to wind tunnel.

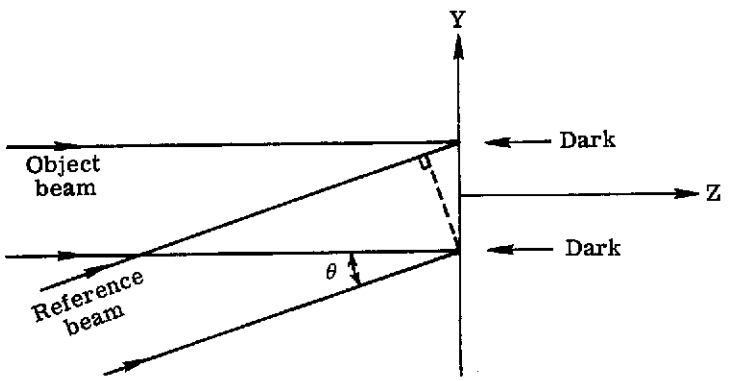

(a) Recording geometry.

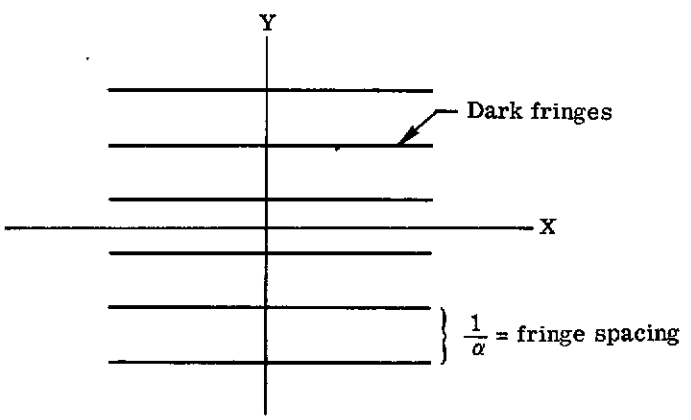

(b) Resulting straight-line fringe pattern.

Figure 10.- Formation of stored holographic grid.

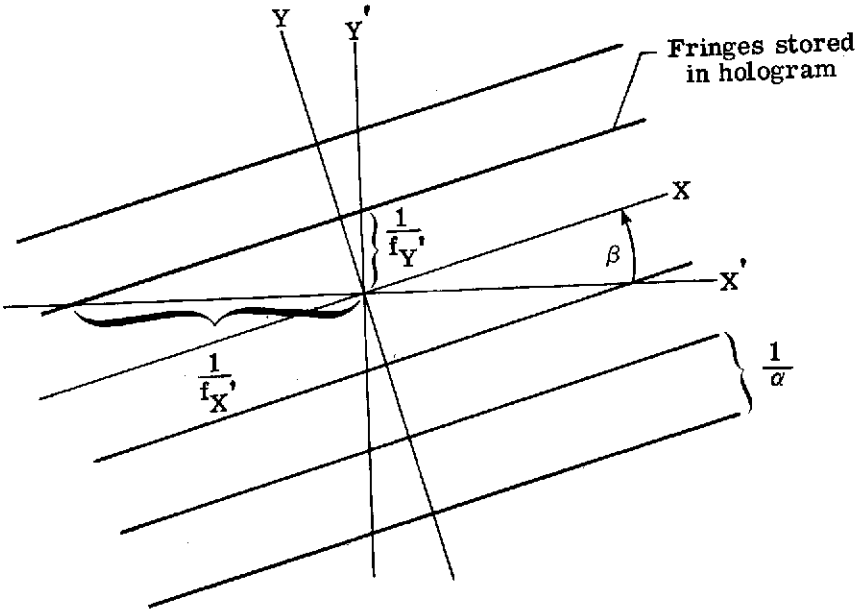

Figure 11.- Geometry for rotated hologram.

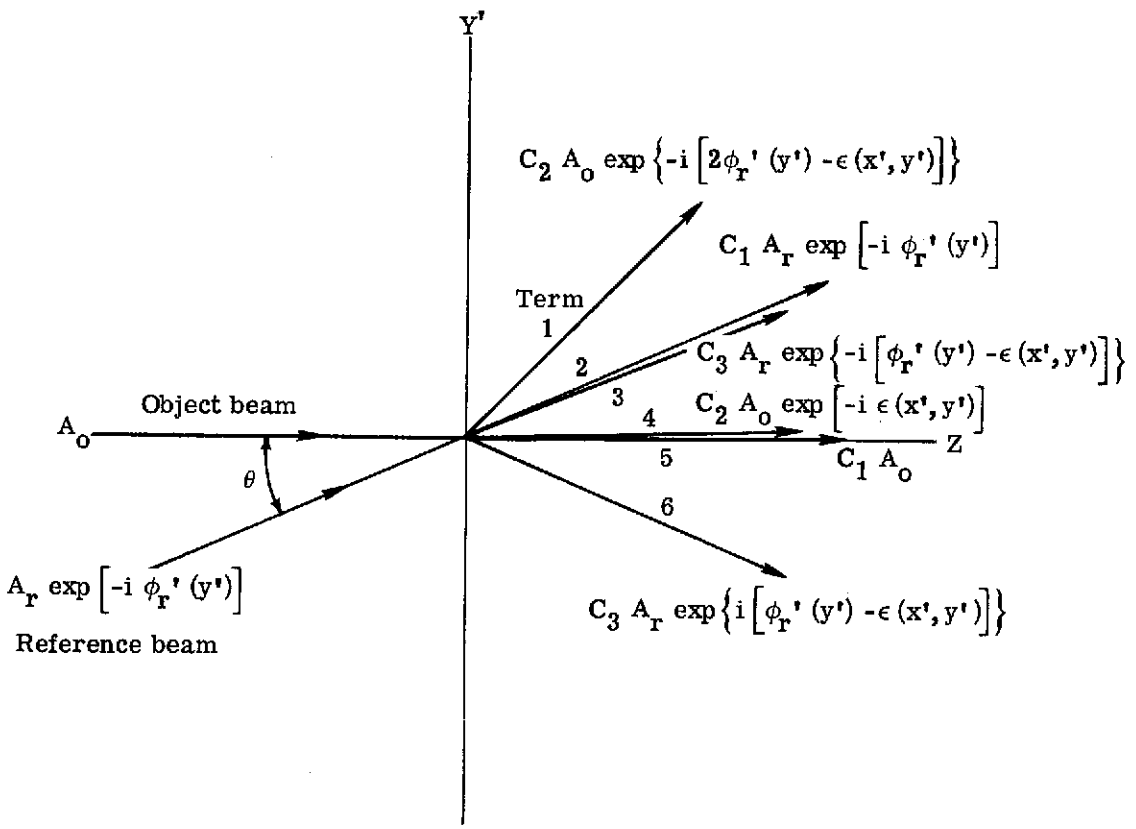

Figure 12.- Reconstruction of rotated hologram with illumination from both reference and object beams. Terms 1 to 6 from expression (A14).

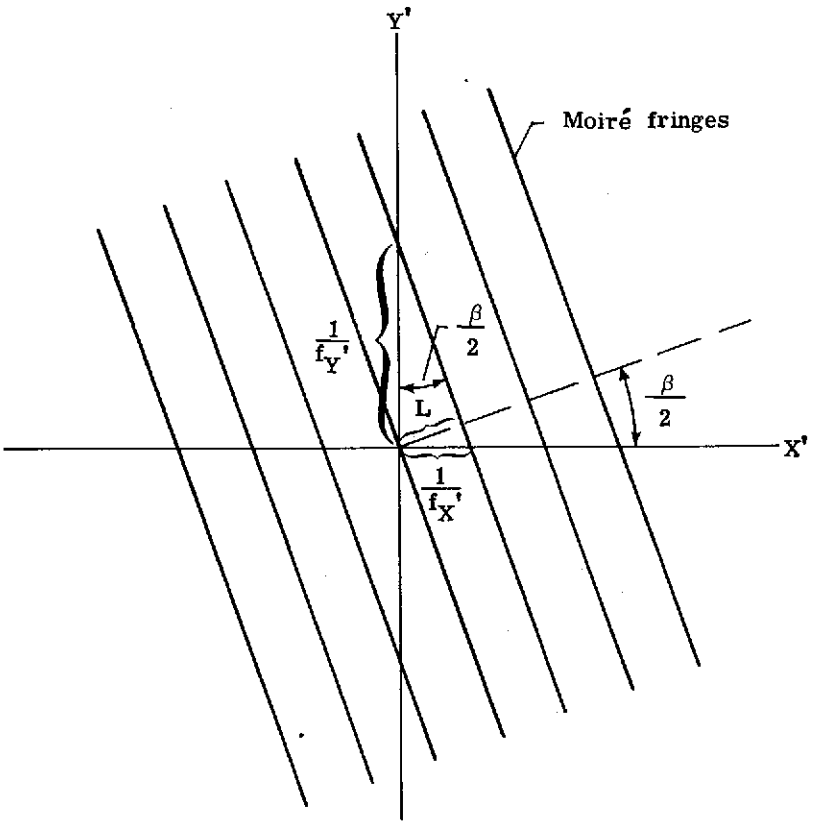

Figure 13.- Spacing and orientation of moiré fringes.

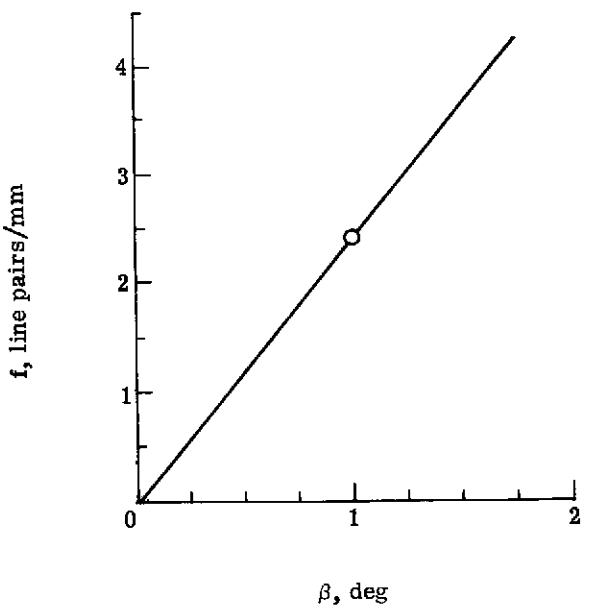

Figure 14.- Spatial frequency of moiré fringes as function of angle of rotation of hologram for $\theta = 5^{o}$, $\lambda_0 = 6328$ Å.

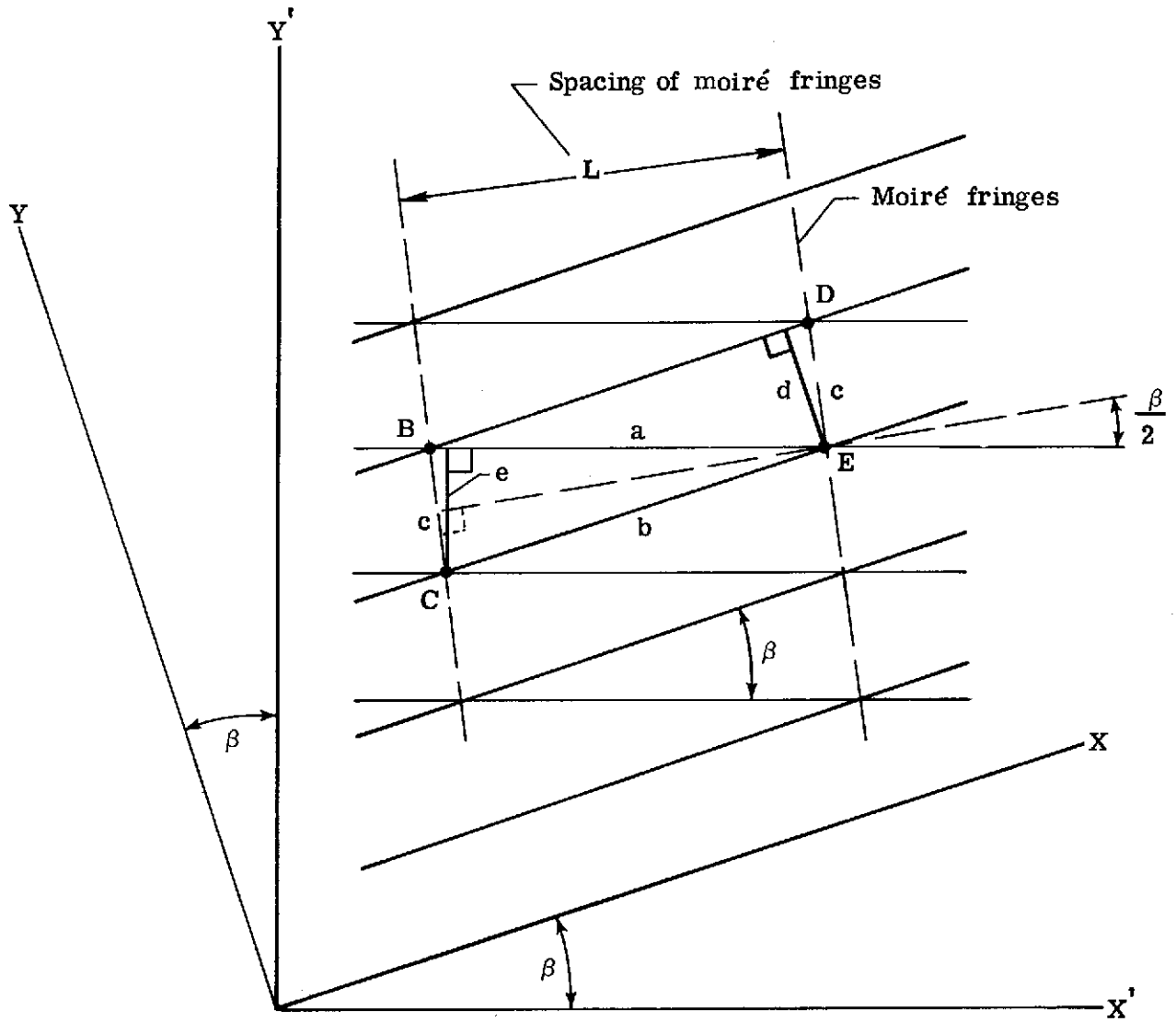

Figure 15.- Geometrical construction of moiré fringes from two grids rotated with respect to one another.